CORRECTIONS POSTED 10 OCTOBER 2023 AND 3 NOVEMBER 2023

SCIENCE ADVANCES | RESEARCH ARTICLE

SPACE SCIENCES

Localized uplift, widespread subsidence, and implications for sea level rise in the New York City metropolitan area

Brett Buzzanga[1]*, David P.S. Bekaert[1], Benjamin D. Hamlington[1], Robert E. Kopp[2], Marin Govorcin[1], Kenneth G. Miller[2]

Regional relative sea level rise is exacerbating flooding hazards in the coastal zone. In addition to changes in the ocean, vertical land motion (VLM) is a driver of spatial variation in sea level change that can either diminish or enhance flood risk. Here, we apply state-of-the-art interferometric synthetic aperture radar and global navigation satellite system time series analysis to estimate velocities and corresponding uncertainties at 30-m resolution in the New York City metropolitan area, revealing VLM with unprecedented detail. We find broad subsidence of 1.6 mm/year, consistent with glacial isostatic adjustment to the melting of the former ice sheets, and previously undocumented hot spots of both subsidence and uplift that can be physically explained in some locations. Our results inform ongoing efforts to adapt to sea level rise and reveal points of VLM that motivate both future scientific investigations into surface geology and assessments of engineering projects.

INTRODUCTION

As Earth's climate warms, the effects of thermal expansion of warming ocean waters and the addition of melting ice from ice sheets and glaciers are causing sea levels to rise on a global scale. Regionally, the amount of sea level rise experienced can vary because of changes in ocean circulation and the solid Earth's gravitational, rotational, and deformational response to melting ice. On a more local scale, an additional driver of spatial variations is the movement of land relative to the ocean. Subsidence or uplift, referred to jointly as vertical land motion (VLM), can either diminish or enhance relative sea level rise (i.e., the rise of sea level relative to the local land surface). Such relative sea level rise poses a substantial threat to the New York City metropolitan area both now and into the future. During the 20th century, relative sea level at the Battery tide gauge in Manhattan, New York City increased at a rate of about 3.1 mm/year. From 2000 to 2022, that rate has increased to 4.4 mm/year. About 1.5 ± 0.2 mm/year of this rate has been attributed to subsidence driven by glacial isostatic adjustment [GIA; (*1*–*3*)]. Projections of future sea level rise from the recent Sixth Assessment Report of the Intergovernmental Panel on Climate Change report (*4*, *5*) show sea levels continuing to increase into the future at an accelerating rate with subsidence continuing to play a key role as a persistent contributor to relative sea level rise.

Protecting coastal populations and assets from coastal flooding is an ongoing challenge for New York City. The combined effect of natural sea level variations and destructive storms is being increasingly exacerbated by ongoing sea level rise. The city has long dealt with coastal flooding from both hurricanes and extratropical storms, but as seen with Superstorm Sandy in 2012, storm surges associated with severe weather events are becoming more destructive because of ongoing sea level rise (*6*, *7*). The relative rise in sea level during the 20th century resulted in an additional $8.1 billion in damages from Sandy than would have occurred a century prior (*2*).

To address the threat posed by sea level rise, New York City has taken steps to increase its resilience. For example, the city has launched a comprehensive plan called "OneNYC" that outlines a range of strategies to adapt to climate change, including improving stormwater management, protecting natural areas, and strengthening infrastructure (*8*). This plan includes actions taken on very local levels, often addressing the threat of impacts at the neighborhood or street unit. In addition, the U.S. Army Corps of Engineers is conducting a feasibility study for a wide range of options to protect New York City and New Jersey from future threats of sea level rise and storms (*9*). To support the actions outlined in these plans, information on ongoing and future relative sea level rise that matches the fine-scale, localized nature of the planning is needed.

For most processes driving sea level rise, any spatial variations are relatively large scale, and a single projection of ice mass loss, ocean circulation change, or thermal expansion is sufficient for all of New York City. Recent studies using space-based observations, however, have shown that VLM can have important spatial variations within a city the size of New York City (*10*, *11*, *12*). In this study, we use interferometric synthetic aperture radar (InSAR) analysis to examine VLM in New York City since 2016. In doing so, broad subsidence—consistent with estimates of GIA—is seen for New York City and its surrounding area. We also identify, however, localized rates of higher subsidence for some areas of critical infrastructure, in addition to areas of previously undocumented uplift that overlap with ongoing environmental projects.

RESULTS AND DISCUSSION

VLM rate estimates from InSAR referenced to global navigation satellite system (GNSS) in the International Terrestrial Reference Frame 2014 [ITRF14; (*13*)] spanning May 2016 to March 2023 (~7 years) reveal broad subsidence throughout the New York City

[1]Jet Propulsion Laboratory, California Institute of Technology, Pasadena, CA 91101, USA. [2]Department of Earth and Planetary Sciences and Rutgers Institute of Earth, Ocean, and Atmospheric Sciences, Rutgers University, New Brunswick, NJ USA.
*Corresponding author. Email: buzzanga@jpl.nasa.gov

metropolitan area (Fig. 1). InSAR rate uncertainties are less than 1.1 mm/year (fig. S1) such that 95.2% of vertical rate velocities in our study area exceed the uncertainty at 1σ (Materials and Methods). InSAR vertical velocities agree well (the root mean square of residuals is 0.7 mm/year) with collocated GNSS station rates estimated using the Median Interannual Difference Adjusted for Skewness (MIDAS) algorithm [(*14*); Materials and Methods and fig. S2].

On average, the New York City metropolitan area is subsiding at a median rate of −1.6 mm/year with a median uncertainty of 0.8 mm/year, in close agreement with the median rate of reprocessed MIDAS GNSS rates (Materials and Methods) of −1.3 mm/year and consistent with GIA estimates from numerical models, which range from −1.8 mm/year (*15*) to −1.0 mm/year (*16*). It is also consistent with estimates of the relative sea level (RSL) contribution due to GIA at the Battery tide gauge [1.5 ± 0.2 mm/year; (*3*)]. There is considerable spatial variability across the study area, with rates ranging from −4.7 mm/year in Essex County to 1.5 mm/year in Queens County (table S1). Within counties and boroughs, Northeastern Staten Island and Manhattan contains the least spatial variability (2.0 mm/year), while Queens contains the most (5.4 mm/year; table S1).

At ~30-m by 30-m posting, our results reveal isolated hot spots of both subsidence and uplift. For example, runway 13/31 at LaGuardia Airport is subsiding at −3.7 ± 0.8 mm/year (Fig. 2A). This runway is built on a former landfill (*17*) and is currently undergoing an $8 billion renovation designed in part to alleviate enhanced flooding from sea level rise. Additional hot spots of subsidence include Arthur Ashe Tennis Stadium (−4.6 ± 0.8 mm/year; fig. S3A), which is built on a landfill and required special construction of a light-weight roof during renovation to reduce subsidence (*18*); highway 440 (−2.8 ± 0.8 mm/year) and interstate 78 (−2.7 ± 0.8 mm/year) in New Jersey (fig. S4, A and A′), which align with historic fill locations (*19*); and the southern portion of Governors Island (−3.4 ± 0.8 mm/year; fig. S4, B and B′), built on 3.5 million m^3 of debris from the subway excavations during the early 20th century (*20*). Hot spots of coastal subsidence are observed in Midland and South Beach (−2.8 ± 0.9 mm/year), in Staten Island at the location of ongoing flood barrier construction (fig. S4, A and A′), as well as on Coney Island (−2.6 ± 0.8 mm/year) and Arverne by the Sea (−3.2 ± 0.9 mm/year) in Queens, both built on artificial fill [(*10*, *17*); fig. S4, C and C′].

Other notable features in the VLM rate map are the two hot spots of uplift in East Williamsburg, Brooklyn (1.6 ± 0.8 mm/year; Fig. 2B) and Woodside, Queens (fig. S3B). The hot spot in East Williamsburg coincides with Newtown Creek, which has long been subject to pollution from raw sewage discharge and industrial activity, including large oil spills in the 1970s and 1990s (*21*). To remove oil from the aquifer beneath Newtown Creek, water pumps have recovered and treated 23 billion liters of groundwater that is discharged to the combined sanitary sewer system [as of 2021; (*21*)]. While groundwater extraction typically leads to land subsidence (*22*), uplift can also occur because of hydrological unloading (*23*). Moreover, the remediation efforts have not been continuous in time and are ongoing (*24*), including at least 750 US Environmental Protection Agency (EPA) underground injection control wells that are used to pump water into the subsurface (fig. S5). These efforts can lead to nonlinearities in VLM that we observe in our time series at Newtown Creek (Fig. 2B), which has a faster upward trend from October 2017 to December 2019 (2.6 ± 0.8 mm/year) than during 2020 to 2023 (1.8 ± 0.8 mm/year). Similarly, VLM in the residential

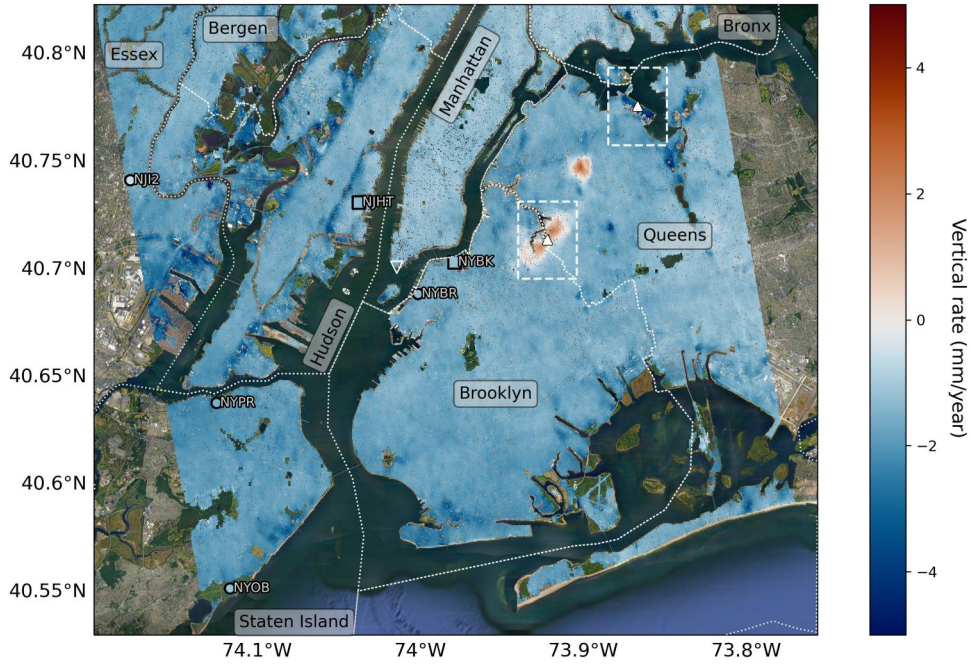

Fig. 1. VLM rate map. Rates are estimated from Sentinel-1–derived interferograms spanning May 2016 to March 2023. Colored square markers indicate GNSS stations used in referencing InSAR velocities to ITRF14, while circles mark stations used in validation. White rectangles and triangles mark the inset maps and time series shown in Fig. 2. White dotted lines show the county/borough borders. The tide gauge in the Battery (Manhattan) is located at the inverted triangle. Corresponding rate uncertainties are found in fig S1.

neighborhood of Woodside, Queens (fig. S3B), built on wetlands drained in the 19th century (*25*), display marked nonlinearity, with a clear period of uplift from May 2016 to December 2019 (6.9 ± 0.9 mm/year) and then no VLM (0.0 ± 0.8 mm/year) for the remainder of the record. Further investigation is required to uncover the specific causes of the uplift, including the magnitude of ongoing injection at wells in the region.

Our findings, performed using cutting-edge InSAR processing techniques (see Materials and Methods), highlight the importance of InSAR in understanding the spatial variability of VLM rates within coastal regions. While other studies have estimated VLM rates from InSAR in New York City, they did not focus on the hot spots observed here. The recent study by Parsons *et al.* (*10*) demonstrates causal links to observed Sentinel-1–derived InSAR subsidence rates from 2015 to 2020 with a mean rate (−1.8 mm/year; consistent with GNSS) and spatial variability (their figure 5A) similar to that found here. However, they do not report clear uplift signals (e.g., Fig. 2B), as they use only six SAR images per year (*26*) rather than exploiting the full dataset (over the study interval). The study in (*11*) highlights New York City in its global analysis, finding spatial variability and the hot spots at Arthur Ashe Stadium and Woodside, Queen. However, as in (*10*), they use a small subset of possible interferometric pairs that results in a dataset noisier than ours (rates ranging from −18.9 to 7.3 mm/year) and lacking data at many of the hot spots we highlight. The dataset from (*27*) covers 2007 to 2020 by combining SAR acquisitions from the Advanced Land Observing Satellite (ALOS1; 2007–2011), Sentinel-1 (2015–2020), and GNSS trends from MIDAS in a joint inversion. Although not directly comparable because of differences in time period and methodology (*28*), their median value in New York City of −1.6 mm/year agrees well with ours (−1.6 mm/year; table 1) and is consistent with GIA. However, they find negligible spatial variability (< 0.5 mm/year over 99.7% of rate estimates) and thus no hot spots of either subsidence or uplift.

Reliable estimates of both the magnitude and spatial variability of VLM are especially important in coastal regions that are increasingly reliant on accurate estimates of sea level change to inform adaptation. GNSS station spacing is too coarse to fully capture the spatial variability of VLM along coastlines (~15 km apart in our study; figs. S4 and S6), so higher-resolution InSAR is necessary for understanding the contribution of VLM to contemporary and future sea level change (*29*). In cities like New York that are actively investing in coastal defenses and infrastructure, precise, high-resolution estimates of VLM can further inform best practices. In

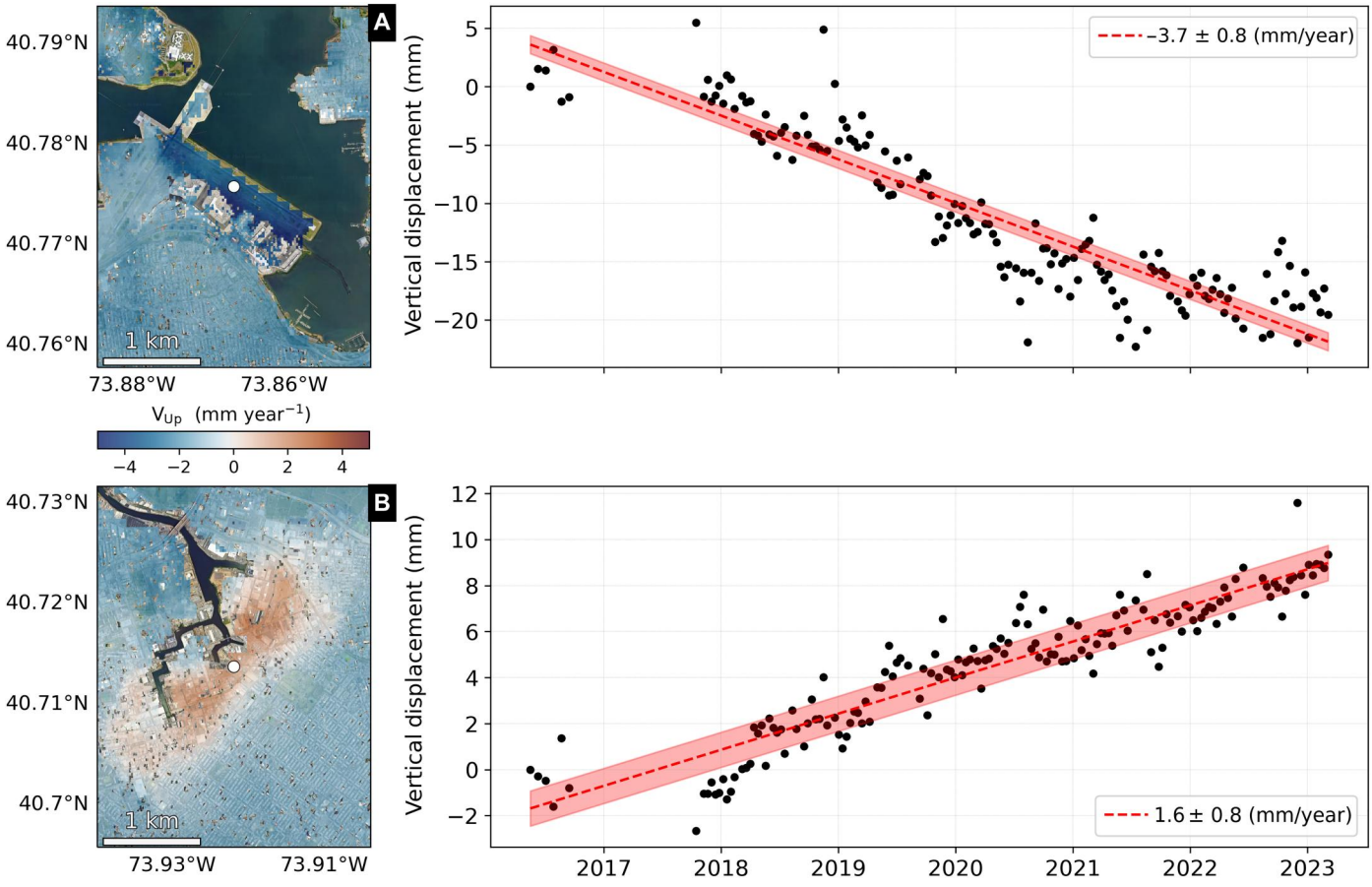

Fig. 2. Hot spots of VLM. Time series are referenced to ITRF14 and relative to the start date (17 May 2016). Dashed red line and shading indicate the linear rate and 1σ uncertainty (see Materials and Methods). (**A**) Runway 13/31 of LaGuardia Airport, Queens (see Fig. 1A for full location), built on a former landfill, and part of a multibillion-dollar upgrade in part to alleviate flooding hazards. (**B**) Newtown Creek in East Williamsburg, Brooklyn, which is undergoing extensive environmental remediation due primarily to the Greenpoint Oil Spill in the late 1970s.

addition, InSAR can reveal hitherto undocumented hot spots, such as the uplift observed at Newtown Creek, that can support future scientific investigations into surface geology and assessments of engineering projects. While specialized expertise is still required for InSAR processing, this is rapidly changing as InSAR standard products become widely available (*30*) and the upcoming release of a North American line-of-sight (LoS) displacement derived from SAR observations by the OPERA project. This will be further enhanced in the coming years with observations from the joint NASA–Indian Space Research Organisation (ISRO) Synthetic Aperture Radar (NISAR) mission, which will observe the U.S. coasts every 12 days with an L-Band sensor better capable of penetrating vegetation than Sentinel-1. In short, high-resolution observations from spaceborne InSAR are an invaluable tool for monitoring and managing a wide variety of natural and anthropogenic changes to Earth's surface.

MATERIALS AND METHODS

We obtained 165 Sentinel-1 single-look complex (SLC) images along track 35 spanning 17 May 2016 to 6 March 2023 from the Alaska Satellite Facility. We prepared them for time series analysis by coregistering them to a single geometry using the ISCE-2 sentinelStack workflow (*31*). Topographic effects are accounted for using the Copernicus GLO30 digital elevation model. We use the state-of-the-art InSAR processing software FRInGE (*32*, *33*) to generate full-resolution (approximately 2.3-m pixels in slant range, 15.6 m in azimuth) wrapped interferograms. FRInGE uses a SqueeSAR-like (*34*) strategy for identifying distributed scatterers and the traditional amplitude dispersion method to identify persistent scatters (*35*, *36*). We identify neighborhoods of statistically self-similar distributed scatters using a window size of 33 pixels in range and 15 lines in azimuth, and an amplitude dispersion threshold of 0.4 for determining persistent scatterer pixels. Moreover, FRInGE uses every possible interferometric pair from the given SAR network to extract the maximum amount of phase information. To improve efficiency, the full time series is split into "mini stacks" of 15 SAR images each, for which the covariance matrix is estimated for each neighborhood of pixels. The covariance matrix is then decomposed into eigenvectors and corresponding eigenvalues. The phase of the largest eigenvector is considered the maximum-likelihood phase estimate and used to generate the wrapped-phase time series (*37*).

We multilook the resulting 164 wrapped interferograms by a factor of 5 × 2. We assume that there are no large phase jumps across water bodies, so we mask and interpolate using inverse distance weighting across them to minimize phase jumps during unwrapping with Snaphu (*38*). The single-reference unwrapped time series phase is converted to displacement by scaling with a factor of $-4\pi/\lambda$, where λ is the Sentinel-1 wavelength (*39*). We estimate LoS velocities by fitting a linear trend plus sinusoid with annual and semiannual components to the displacement time series. The LoS velocity uncertainty is the SD of the regression slope (*40*). While a linear model is suitable for most of the region subsiding because of the steady rate of GIA, it can lead to underestimations of nonlinear deformation (e.g., at Woodside; fig. S43B) and the uncertainty of the model. We geocode our results to a posting of approximately 30 m × 30 m.

We apply geophysical and geometrical corrections using MintPy [fig. S1; (*40*)]. We first correct for atmospheric effects using ERA5 reanalysis with PyAPS (*41*), solid earth tides with PySolid (*42*) and topographic residuals (*43*). We then remove long-wavelength horizontal motion due to plate tectonics using the model for the North American plate (*44*). We remove outliers in the InSAR time series by dropping SAR acquisitions outside of the 95% confidence interval (*45*). We empirically reduce residual noise using empirical orthogonal function analysis (*46*) by decomposing the time series into orthogonal eigenvectors and reconstructing it using only the leading 20 vectors that contain 87% of the variance. Note that we remove an annual and semiannual cycle from the time series by fitting a sinusoid before decomposition.

The total effect of applied corrections is small: Averaged over the study area, velocities are 0.1 mm/year lower than before the correction, and 99.7% of residual velocities are between −0.4 and 0.2 mm/year (fig. S7A). Uncertainty is reduced on average by less than 0.1 mm/year (fig. S7B), with a maximum reduction (pixel-wise) of 0.3 mm/year. This is expected given the small size and flat terrain of the study area relative to the long-wavelength spatially correlated tropospheric noise (*29*), and coarse resolution of the ERA5 weather model [31 km; (*47*)]. We only consider coherent pixels [temporal coherence greater than 0.8; (*48*)] and those on land according to the watermask available from Open Street Maps (*49*).

We leverage the GNSS network to tie our relative InSAR LoS velocity into the terrestrial reference frame. There are nine GNSS stations in our study available from the Nevada Geodetic Lab (*50*) with MIDAS velocity and uncertainty estimates; however, they vary in data quality and record lengths. We perform additional screening of the GNSS time series to obtain GNSS velocities and corresponding uncertainties suitable for comparison to our InSAR rates. For GNSS stations that experienced nonlinear steps in the time series due to equipment changes or deformation, we recompute a rate and uncertainty using the MIDAS algorithm for a linear temporal interval (fig. S8). We then discard stations without measurements on at least 40% of the days during the SAR sensing period (10 May 2016 to 6 March 2023; the six remaining stations considered are shown in Fig. 1). We also discard the GNSS station on the tide gauge, NYBP, which has numerous step changes that make the rate calculation sensitive to the GNSS processing strategy and rate estimation by up to 50% (*14*, *51*, *52*).

Because of limited constraints in decomposing satellite LOS with only one viewing SAR geometry, we projected our corrected LoS displacements to the vertical by assuming horizontal motion to be negligible. We take this assumption to be justified in this case as we removed known contributors to large-scale horizontal land motion: solid Earth tides and rigid plate motion (*44*). Also, there is negligible horizontal motion indicated by GNSS stations after removing plate motion (*53*), as well as large-scale horizontal motion due to GIA (*16*) (0.03 mm/year per 100 km in satellite LoS; fig. S9). However, if localized horizontal motion exists, then it could propagate and bias VLM estimates. We obtained vertical rates using the equation

$$V_{\mathrm{Up}} = \frac{V_{\mathrm{LOS}}}{\cos\,(\theta)} \tag{1}$$

where θ is the local incidence angle. We tie Brooklyn and Queens in the western portion of our study area to the GNSS station NYBK and New Jersey and Staten Island to GNSS station NJHT (fig.

S10). We then add the GNSS velocity to its corresponding portion of InSAR rates and propagate the uncertainty (*54*) to obtain our final velocity and uncertainty estimates. In the overlap regions (Manhattan and Bronx), which are approximately equidistant from the two reference stations, we average pixels weighted by the InSAR uncertainty. Using two stations reduces unwrapping errors caused by water bodies separating the region, and constraints additional mid-wavelength signals that could lead to biases when considering a single station (fig. S10). To reduce spatially correlated and local scattering noise, the vertical time series shown in Fig. 2 and fig. S3 are the displacement history relative to a nearby (~2 km) stable (|vertical rate| < 0.1 mm/year) reference location.

Correction (10 October 2023): Due to a typographical error, "Newtown Creek" was incorrectly spelled as "Newton Creek" in the main text of the article and the Supplementary Materials. This has been corrected and the XML, PDF, and Supplementary Materials files have been updated.

Correction (1 November 2023): Due to a production error, the label "-3.7 +/- 0.8 (mm/year)" in Fig. 2A was incorrectly changed to "-37 +/- 0.8 (mm/year)". This has been reverted to the correct "-3.7". Additionally, the Data and Materials Availability statement has been updated to include a link to the authors' data on Dryad.

Supplementary Materials

This PDF file includes:

Figs. S1 to S10
Tables S1 and S2
References

REFERENCES AND NOTES

1. R. E. Kopp, R. M. Horton, C. M. Little, J. X. Mitrovica, M. Oppenheimer, D. J. Rasmussen, B. H. Strauss, C. Tebaldi, Probabilistic 21st and 22nd century sea-level projections at a global network of tide-gauge sites. *Earth's Future* **2**, 383–406 (2014).
2. K. G. Miller, R. E. Kopp, B. P. Horton, J. V. Browning, A. C. Kemp, A geological perspective on sea-level rise and its impacts along the U.S. mid-Atlantic coast. *Earth's Future* **1**, 3–18 (2013).
3. G. G. Garner, T. Hermans, R. E. Kopp, A. B. A. Slangen, T. L. Edwards, A. Levermann, S. Nowicki, M. D. Palmer, C. Smith, B. Fox-Kemper, H. T. Hewitt, C. Xiao, G. Aðalgeirsdóttir, S. S. Drijfhout, N. R. Golledge, M. Hemer, G. Krinner, A. Mix, D. Notz, I. S. Nurhati, B. Pearson, IPCC AR6 sea level projections. *Zenodo* (2021); https://doi.org/10.5281/zenodo.5914709.
4. B. Fox-Kemper H. T. Hewitt, C. Xiao, G. Aðalgeirsdóttir, S. S. Drijfhout, T. L. Edwards, N. R. Golledge, M. Hemer, R. E. Kopp, G. Krinner, A. Mix, D. Notz, S. Nowicki, I. S. Nurhati, L. Ruiz, J. B. Sallée, A. B. A. Slangen, Y. Yu, in *Climate Change 2021: The Physical Science Basis. Contribution of Working Group I to the Sixth Assessment Report of the Intergovernmental Panel on Climate Change*, V. Masson-Delmotte P. Zhai, A. Pirani, S. L. Connors, C. Péan, S. Berger, N. Caud, Y. Chen, L. Goldfarb, M. I. Gomis, M. Huang, K. Leitzell, E. Lonnoy, J. B. R. Matthews, T. K. Maycock, T. Waterfield, O. Yelekci, R. Yu, B. Zhou, Eds. (Cambridge Univ. Press, 2021), pp. 1211–1362.
5. G. Garner, T. H. J. Hermans, R. Kopp, A. Slangen, T. Edwards, A. Levermann, S. Nowicki, M. D. Palmer, C. Smith, B. Fox-Kemper, H. Hewitt, C. Xiao, G. Aðalgeirsdóttir, S. Drijfhout, N. Golledge, M. Hemer, G. Krinner, A. Mix, D. Notz, I. Nurhati, B. Pearson, IPCC AR6 WGI Sea Level Projections, *World Data Center for Climate (WDCC) at DKRZ* (2023); 10.26050/wdcc/ar6.ipcc-ddc_ar6_sup_slpr.
6. V. Gornitz, M. Oppenheimer, R. Kopp, R. Horton, P. Orton, C. Rosenzweig, W. Solecki, L. Patrick, Enhancing New York City's resilience to sea level rise and increased coastal flooding. *Urban Clim.* **33**, 100654 (2020).
7. M. Bloomberg, A Stronger, More Resilient New York (PlaNYC Report, 2013).
8. The City of New York, *OneNYC 2050: Building a Strong and Fair City* (2019).
9. U.S. Army Corps of Engineers, New York-New Jersey Harbor and Tributaries Coastal Storm Risk Management Feasability Study (2022).
10. T. Parsons, P.-C. Wu, M. (. M.). Wei, S. D'Hondt, The weight of new york city: Possible contributions to subsidence from anthropogenic sources. *Earth's Future* **11**, e2022EF003465 (2023).
11. C. Tay, E. O. Lindsey, S. T. Chin, J. W. McCaughey, D. Bekaert, M. Nguyen, H. Hua, G. Manipon, M. Karim, B. P. Horton, T. Li, E. M. Hill, Sea-level rise from land subsidence in major coastal cities. *Nat. Sustain* **5**, 1049–1057 (2022).
12. B. A. Brooks, M. A. Merrifield, J. Foster, C. L. Werner, F. Gomez, M. Bevis, S. Gill, Space geodetic determination of spatial variability in relative sea level change, Los Angeles basin. *Geophys. Res. Lett.* **34**, 10.1029/2006GL028171 (2007).
13. Z. Altamimi, P. Rebischung, L. Métivier, X. Collilieux, ITRF2014: A new release of the International Terrestrial Reference Frame modeling nonlinear station motions. *J. Geophys. Res. Solid Earth* **121**, 6109–6131 (2016).
14. G. Blewitt, C. Kreemer, W. C. Hammond, J. Gazeaux, MIDAS robust trend estimator for accurate GPS station velocities without step detection. *J. Geophys. Res. Solid Earth* **121**, 2054–2068 (2016).
15. W. R. Peltier, D. F. Argus, R. Drummond, Comment on "An Assessment of the ICE-6G_C (VM5a) Glacial Isostatic Adjustment Model" by Purcell et al. *J. Geophys. Res. Solid Earth* **123**, 2019–2028 (2018).
16. L. Caron, E. R. Ivins, E. Larour, S. Adhikari, J. Nilsson, G. Blewitt, GIA model statistics for GRACE hydrology, cryosphere, and ocean science. *Geophys. Res. Lett.* **45**, 2203–2212 (2018).
17. D. C. Walsh, R. G. LaFleur, Landfills in New York City: 1844–1994. *Groundwater* **33**, 556–560 (1995).
18. T. Newcomb, Well Look At That—Arthur Ashe Stadium is Getting a Roof. And It's Made of Fabric (2013); www.si.com/extra-mustard/2013/08/15/well-look-at-that-arthur-ashe-stadium-is-getting-a-roof-and-its-made-of-fabric#gid=ci0255c6907001279d&pid=b_14aug13_437_ashejpg.
19. New Jersey Department of Environmental Protection and New Jersey Geological and Water Survey, Historic Fill For New Jersey As Of March 2018 (2018).
20. The History of Governors Island; www.govisland.com/history.
21. New York State Department of Environmental Conservation, Greenpoint Petroleum Remediation Project (2022).
22. M. Shirzaei, J. Freymueller, T. E. Törnqvist, D. L. Galloway, T. Dura, P. S. J. Minderhoud, Measuring, modelling and projecting coastal land subsidence. *Nat. Rev. Earth Environ.* **2**, 40–58 (2021).
23. J. Overacker, W. C. Hammond, G. Blewitt, C. Kreemer, Vertical land motion of the high plains aquifer region of the united states: Effect of aquifer confinement style, climate variability, and anthropogenic activity. *Water Resour. Res.* **58**, e2021WR031635 (2022).
24. United States Environmental Protection Agency, *Superfund Record of Decision: Operable Unit 2 Newtown Creek Superfund Site* (United States Environmental Protection Agency Region 2 New York, 2020).
25. Kelly, Frank Bergen, the City History Club of New York, *Historical Guide to the City of New York* (FA Stokes Company, 1909).
26. P. Wu, M. (. M.). Wei, S. D'Hondt, Subsidence in coastal cities throughout the world observed by inSAR. *Geophys. Res. Lett.* **49**, e2022GL098477 (2022).
27. L. Ohenhen, M. Shirzaei, C. Ojha, M. Kirwan, VLM and Horizontal Velocity Data for US Atlantic Coast. University Libraries, Virginia Tech, 10.7294/19350959.v3 (2023).
28. M. Shirzaei, A Wavelet-Based Multitemporal DInSAR Algorithm for Monitoring Ground Surface Motion. *IEEE Geosci. Remote Sensing Lett.* **10**, 456–460 (2013).
29. D. P. S. Bekaert, C. E. Jones, K. An, M.-H. Huang, Exploiting UAVSAR for a comprehensive analysis of subsidence in the Sacramento Delta. *Remote Sens. Environ.* **220**, 124–134 (2019).
30. S. S. Sangha, N. Arenas, M. G. Bato, D. P. Bekaert, B. A. Buzzanga, R. Gens, J. H. Kennedy, A. Johnston, E. Havazli, K. Hogenson, Others, in *AGU Fall Meeting Abstracts* (2022), vol. 2022, pp. ED12C-0370.
31. H. Fattahi, P. Agram, M. Simons, A network-based enhanced spectral diversity approach for TOPS time-series analysis. *IEEE Trans. Geosci. Remote Sens.* **55**, 777–786 (2017).
32. E. Tymofyeyeva, P. S. Agram, H. Fattahi, D. P. Bekaert, in *AGU Fall Meeting Abstracts* (2019), vol. 2019, pp. T13D-0304.
33. H. Fattahi, P. S. Agram, E. Tymofyeyeva, D. P. Bekaert, in *AGU Fall Meeting Abstracts* (2019), vol. 2019, pp. G11B-0514.
34. A. Ferretti, A. Fumagalli, F. Novali, C. Prati, F. Rocca, A. Rucci, A new algorithm for processing interferometric data-stacks: SqueeSAR. *IEEE Trans. Geosci. Remote Sens.* **49**, 3460–3470 (2011).
35. A. Ferretti, C. Prati, F. Rocca, Permanent scatterers in SAR interferometry. *IEEE Trans. Geosci. Remote Sens.* **39**, 8–20 (2001).
36. A. Hooper, D. Bekaert, K. Spaans, M. Arıkan, Recent advances in SAR interferometry time series analysis for measuring crustal deformation. *Tectonophysics* **514-517**, 1–13 (2012).
37. H. Ansari, F. De Zan, R. Bamler, Sequential estimator: Toward efficient InSAR time series analysis. *IEEE Trans. Geosci. Remote Sens.* **55**, 5637–5652 (2017).

38. C. W. Chen, H. A. Zebker, Phase unwrapping for large SAR interferograms: Statistical segmentation and generalized network models. *IEEE Trans. Geosci. Remote Sens.* **40**, 1709–1719 (2002).
39. R. F. Hanssen, *Radar Interferometry: Data Interpretation and Error Analysis* (Springer Science & Business Media, 2001).
40. H. Fattahi, F. Amelung, InSAR bias and uncertainty due to the systematic and stochastic tropospheric delay. *J. Geophys. Res. Solid Earth.* **120**, 8758–8773 (2015).
41. R. Jolivet, R. Grandin, C. Lasserre, M. P. Doin, G. Peltzer, Systematic InSAR tropospheric phase delay corrections from global meteorological reanalysis data. *Geophys. Res. Lett.* **38** 10.1029/2011GL048757, (2011).
42. Y. Zhang, H. Fattahi, X. Pi, P. Rosen, M. Simons, P. Agram, Y. Aoki, Range geolocation accuracy of C-/L-Band SAR and its implications for operational stack coregistration. *IEEE Trans. Geosci. Remote Sens.* **60**, 1–19 (2022).
43. H. Fattahi, F. Amelung, DEM error correction in insar time series. *IEEE Trans. Geosci. Remote Sens.* **51**, 4249–4259 (2013).
44. O. L. Stephenson, Y. Liu, Y. Zhang, M. Simons, P. Rosen, X. Xu, The impact of plate motions on long-wavelength inSAR-derived velocity fields. *Geophys. Res. Lett.* **49**, e2022GL099835 (2022).
45. Y. Zhang, H. Fattahi, F. Amelung, Small baseline InSAR time series analysis: Unwrapping error correction and noise reduction. *Comput. Geosci.* **133**, 104331 (2019).
46. E. Chaussard, R. Bürgmann, M. Shirzaei, E. J. Fielding, B. Baker, Predictability of hydraulic head changes and characterization of aquifer-system and fault properties from InSAR-derived ground deformation. *J. Geophys. Res. Solid Earth* **119**, 6572–6590 (2014).
47. A. Parizzi, R. Brcic, F. De Zan, InSAR performance for large-scale deformation measurement. *IEEE Trans. Geosci. Remote Sens.* **59**, 8510–8520 (2021).
48. A. Pepe, R. Lanari, On the Extension of the Minimum Cost Flow Algorithm for Phase Unwrapping of Multitemporal Differential SAR Interferograms. *IEEE Trans. Geosci. Remote Sens.* **44**, 2374–2383 (2006).
49. OpenStreetMap Contributors, Planet dump retrieved from https://planet.osm.org on 1 January 2023 (2017).
50. G. Blewitt, W. Hammond, C. Kreemer, Harnessing the GPS data explosion for interdisciplinary science. *Eos Trans. Am. Geophys. Union* **99**, 10.1029/2018EO104623, (2018).
51. M. Gravelle, G. Wöppelmann, K. Gobron, Z. Altamimi, M. Guichard, T. Herring, P. Rebischung, The ULR-repro3 GPS data reanalysis and its estimates of vertical land motion at tide gauges for sea level science. *Earth Syst. Sci. Data* **15**, 497–509 (2023).
52. B. Männel, T. Schöne, M. Bradke, H. Schuh, Vertical Land Motion at Tide Gauges Observed by GNSS: A New GFZ-TIGA Solution, in *International Association of Geodesy Symposia* (Springer, Berlin, Heidelberg, 2022); https://doi.org/10.1007/1345_2022_150.
53. G. Blewitt, C. Kreemer, W. C. Hammond, J. M. Goldfarb, Terrestrial reference frame NA12 for crustal deformation studies in North America. *J. Geodyn.* **72**, 11–24 (2013).
54. D. P. S. Bekaert, B. D. Hamlington, B. Buzzanga, C. E. Jones, Spaceborne synthetic aperture radar survey of subsidence in hampton roads, Virginia (USA). *Sci. Rep.* **7**, 14752 (2017).
55. U.S. Army Corps of Engineers, New York District, FACT SHEET - South Shore of Staten Island, N.Y. (2023).
56. C. Wilkinson, Berry Bits: Brennan Field Reconstruction Underway (2020).
57. The New York Public Library, The Changing Shoreline of NYC; spacetime.nypl.org/the-changing-shoreline-of-nyc/.

Acknowledgments: We acknowledge the European Union Commission and European Space Agency for providing the Sentinel-1 images through the Alaska Satellite Facility for free, the European Centre for Medium-Range Weather Forecasts for the ERA5 products, and the Nevada Geodetic laboratory for providing the GNSS data. We thank the GNSS community and NOAA for maintaining the networks and sharing observations. We specifically thank the following people/agencies for maintaining the GNSS stations: J. Savarese and the NYC Department of Design and Construction (NYBK, NYOB, and NYPR), B. Morris, J. Greenfield, SmartNet North America, and the New Jersey Institute of Technology (NJHT and NJI2). We thank H. Stanfield and the EPA for providing information regarding the injection well activity at Newtown Creek. We appreciate the insightful comments provided by one anonymous reviewer, A. Hooper, and B. Hammond that greatly improved this manuscript. The research was carried out in part at the Jet Propulsion Laboratory, California Institute of Technology, under a contract with the National Aeronautics and Space Administration. Copyright: 2023. All rights reserved. **Funding:** This study was supported by ROSES New Investigator Program grant (D.P.S.B. and B.B.), NASA Sea Level Change Team (B.D.H. and R.E.K.), NISAR Science Team (D.P.S.B.), and OPERA (M.G.). **Author contributions:** Conceptualization: D.P.S.B., B.B., and B.D.H. Methodology: B.B., D.P.S.B., and M.G. Investigation: B.B., B.D.H., and R.E.K. Visualization: B.B. Supervision: D.P.S.B. and B.D.H. Writing—original draft: B.B. and B.D.H. Writing—review and editing: D.P.S.B., R.E.K., K.G.M., and M.G. **Competing interests:** The authors declare that they have no competing interests. **Data and materials availability:** All data needed to evaluate the conclusions in the paper are present in the paper and/or the Supplementary Materials. InSAR processing software is freely available on GitHub and archived on Zenodo. ISCE-2 is at https://github.com/isce-framework/isce2 and https://zenodo.org/record/8157051, FRInGE is at https://github.com/isce-framework/fringe/tree/main and https://zenodo.org/record/8157065, and MintPy is at https://github.com/insarlab/MintPy and https://zenodo.org/record/7502839. GNSS data and MIDAS rates and uncertainties are available from the Nevada Geodetic Lab at http://geodesy.unr.edu. Sentinel-1 SLC images are available at the Alaska Satellite Facility Distributed Active Archive Center (https://asf.alaska.edu/). The rate and associated uncertainty map produced in this work are available at Dryad at https://doi.org/10.5061/dryad.cz8w9gj85.

Submitted 19 May 2023
Accepted 15 August 2023
Published 27 September 2023
10.1126/sciadv.adi8259